

Reference compounds for characterizing cellular injury in

high-content cellular morphology assays

Jayme L. Dahlin^{1#*}, Bruce K. Hua^{2#}, Beth E. Zucconi³, Shawn D. Nelson Jr.⁴, Shantanu Singh⁵,
Anne E. Carpenter⁵, Jonathan H. Shrimp⁶, Evelyne Lima-Fernandes⁷, Mathias J. Wawer²,
Lawrence P.W. Chung², Ayushi Agrawal², Mary O'Reilly⁸, Dalia Barsyte-Lovejoy⁷, Magdalena
Szewczyk⁷, Fengling Li⁷, Parnian Lak⁹, Matthew Cuellar¹⁰, Philip A. Cole³, Jordan L. Meier⁶, Tim
Thomas¹¹, Jonathan B. Baell¹², Peter J. Brown⁷, Michael A. Walters¹⁰, Paul A. Clemons², Stuart
L. Schreiber², Bridget K. Wagner^{2*}

Author affiliations

¹ National Center for Advancing Translational Sciences, National Institutes of Health, Rockville, MD, USA

² Chemical Biology and Therapeutics Science Program, Broad Institute, Cambridge, MA, USA

³ Division of Genetics, Departments of Medicine and Biological Chemistry and Molecular Pharmacology, Harvard Medical School and Brigham and Women's Hospital, Boston, MA, USA

⁴ Stanley Center, Broad Institute, Cambridge, MA, USA

⁵ Imaging Platform, Broad Institute, Cambridge, MA, USA

⁶ Chemical Biology Laboratory, Center for Cancer Research, National Cancer Institute, National Institutes of Health, Frederick, MD, USA

⁷ Structural Genomics Consortium, University of Toronto, Toronto, ON, Canada

⁸ Pattern, Broad Institute, Cambridge, MA, USA

⁹ Department of Pharmaceutical Chemistry and Quantitative Biology Institute, University of California San Francisco, San Francisco, CA, USA

¹⁰ Institute for Therapeutics Discovery and Development, University of Minnesota, Minneapolis, MN, USA

¹¹ Department of Medical Biology, University of Melbourne, Parkville, VIC, Australia

¹² Medicinal Chemistry Theme, Monash Institute of Pharmaceutical Sciences, Monash University, Parkville, VIC, Australia

[#], equal contributions

Corresponding authors (*)

Chemical Biology and Therapeutics Science Program, Broad Institute, 415 Main Street, Cambridge, Massachusetts, 02142, USA; (e) bwagner@broadinstitute.org

National Center for Advancing Translational Sciences, National Institutes of Health, 9800 Medical Center Drive, Rockville, Maryland, 20850, USA; (e) jayme.dahlin@nih.gov

Abstract

Robust, generalizable approaches to identify compounds efficiently with undesirable mechanisms of action in complex cellular assays remain elusive. Such a process would be useful for hit triage during high-throughput screening and, ultimately, predictive toxicology during drug development. We generated cell painting and cellular health profiles for 218 prototypical cytotoxic and nuisance compounds in U-2 OS cells in a concentration-response format. A diversity of compounds causing cellular damage produced bioactive cell painting morphologies, including cytoskeletal poisons, genotoxins, nonspecific electrophiles, and redox-active compounds. Further, we show that lower quality lysine acetyltransferase inhibitors and nonspecific electrophiles can be distinguished from more selective counterparts. We propose that the purposeful inclusion of cytotoxic and nuisance reference compounds such as those profiled in this *Resource* will help with assay optimization and compound prioritization in complex cellular assays like cell painting.

Introduction

Cellular “nuisance” compounds are a significant burden in high-throughput screening (HTS), high-content screening (HCS), and chemical biology. These compounds can appear to be bioactive yet act through nonspecific and poorly optimizable mechanisms of action (MoA) such as redox cycling, reversible covalent bond formation, nonselective reactivity, and cytotoxicity^{1,2}. Compounds causing cellular damage by more specific MoAs (e.g., tubulin and electron-transport chain poisons) can also be undesirable in certain contexts. Thus, cell-active compound prioritization can be difficult due to the uncertainty regarding the mechanism(s) producing phenotypic readouts³. Cell-free assays for compound-dependent interferences are helpful, but they may not model the ideal conditions for compound-mediated interference, such as xenobiotic metabolism or specific cellular microenvironments^{4,5}. Instead, investigating cell-active compound MoA usually requires resource-intensive cellular assays that may also need extensive customization. Therefore, simple tools and resources, applicable to many areas of biology, which would help prioritize chemical matter in cell-based assays without requiring extensive counter-screening are needed.

We previously participated in the development of an unbiased, multiplexed high-content cellular morphology assay (“Cell Painting”, CP) which labels DNA, ER, nucleoli, cytoplasmic RNA, F-actin, Golgi apparatus, plasma membrane, and mitochondria⁶⁻⁸. The CP assay has been used for its strong information content while being higher in throughput and lower in cost relative to other profiling techniques like transcriptomics⁹. Mechanistic hypotheses can be inferred from CP data when compounds share similar phenotypic profiles¹⁰⁻¹³. Many groups have used CP to biologically annotate novel synthetic and other chemical libraries¹⁴⁻¹⁸.

An acknowledged and challenging aspect of HTS is that many cell-active compounds that emerge as hits result from undesirable MoAs¹⁹. Effective triage of such chemical matter typically involves an extensive post-screening cascade of secondary and tertiary assays. Despite

widespread use of HCS, there are still many unanswered questions about the best practices and limitations of these assays, including CP, as it pertains to addressing undesirable as well as cytotoxic/cytostatic chemical matter. The US Environmental Protection Agency used image-based profiles from the cell painting assay to characterize selected environmental chemicals' bioactivity and toxicity, compared to more expensive chemical safety assessments²⁰ and PROTACs have been tested for mitotoxicity using cell painting²¹. Groups have developed customized assays to detect nephrotoxicity, pulmonotoxicity, and other toxicities using specialized cell models and stains for each^{22,23}. We previously developed two cell health assays using specific stains and antibodies and found, using CRISPR reagents targeting various cancer-related genes, that many of their outcomes can be predicted using the information in cell painting images²⁴. None of these assays have been tested in the context of a broad set of cytotoxic and nuisance compounds.

We therefore profiled a series of prototypical cytotoxic and nuisance compounds by the established CP assay to characterize systematically outcomes associated with compound-dependent cellular injury. These results demonstrate the utility of this approach in distinguishing low- from high-quality chemical matter, and provide a blueprint for routinely detecting nuisance compounds in triage activities during HTS.

Results

Characterization of cellular injury using cell painting

Retrospective analysis of public data from 30,616 compounds profiled by cell painting (CP) at 10 μ M concentrations as part of the NIH Molecular Libraries Initiative (MLI) showed that wells with low cell counts tend to have strong phenotypes in the CP assay (**Figure 1a**)²⁵. Similar

trends have also been described previously¹⁷. Given this relationship between cellular health and bioactive morphology, we independently performed CP on 218 cytotoxins and prototypical nuisance compounds in quantitative HTS (qHTS, or concentration-response) format with a typical concentration range of 0.6 to 20 μ M²⁶. The extracted morphological features were subjected to feature reduction, unsupervised hierarchical clustering, and principal component analysis (PCA). Notably, cell features directly and indirectly based on cell numbers were excluded from these analyses. Compounds associated with several cellular injury mechanisms produced distinct morphological clusters (e.g., tubulin poisons [cluster 8], genotoxins [cluster 6]; **Figure 1b, c; Supplementary Figure 1**). Other classes were less active, possibly because nonspecific binding may occur only at concentrations higher than the 20 μ M maximum concentration profiled here (i.e., tannins, saponins). The cluster with the most variance and occupying the largest area in the PCA plot was associated with a diversity of compounds causing gross cellular injury such as nonspecific electrophiles (“NSEs”), proteasome inhibitors, and miscellaneous cytotoxins (cluster 9, “gross injury”; **Figure 1b, c**). As expected, CP activity score and clustering were inversely correlated with cell number in this panel of cytotoxic compounds (**Figure 1d**), even more so than in the diverse panels of small molecules previously studied.

To estimate generalizability, we analyzed the existing MLI dataset for correlation to clusters 1-9 from our independent profiling of cytotoxins and nuisance compounds, using the shared extracted features between the two datasets (**Figure 1e**). We then prospectively re-tested 285 compounds from the MLI dataset with either high (MLI-HC) or no correlation (MLI-NC) to the gross injury phenotype (cluster 9; **Supplementary Figure 2**)²⁵. We found that 98/119 (82%) and 21/166 (13%) of MLI-HC and MLI-NC compounds, respectively, were called bioactive upon retesting (**Figure 1e**). These results suggest that characterizing the phenotypic signatures of

nuisance and cellular injury compounds could be used to alert scientists about potential compound liabilities of HCS-bioactive compounds.

Analysis of select compounds suggested these CP phenotypes are robust across independent experiments (mean correlation = 0.87 ± 0.06 ; **Supplementary Figure 3**). Closer inspection of individual compound profiles corroborated these general observations (**Figure 1f**). These data demonstrate that prototypical cytotoxic compounds produce significant and diverse CP-defined phenotypes.

Electrophiles and cell painting phenotypes

Given the growing interest in targeted electrophiles (TEs) in drug discovery and chemical biology²⁷, we then profiled a series of NSEs, inactive analogs (NSE-IAs), and 13 high-quality TEs targeting a variety of proteins (e.g., BTK, EGFR, FGFR, KRAS Δ G12C)²⁷. Amongst this electrophile-focused subset, CP activity was also inversely correlated with cell number after compound treatment (**Figure 2a**). PCA revealed that most of the NSEs and some TEs occupied the gross cell injury feature spaces, but only at compound concentrations $\geq 10 \mu\text{M}$, whereas most NSE-IAs were inactive (**Figure 2b**). Notably, some of the TE targets are absent (KRAS G12C) or not highly expressed (BTK) in the profiled U-2 OS cells. Many NSEs (13/18, 72%), a subset of TEs (3/13, 23%), and only one NSE-IA (1/14, 7%) occupied the gross injury cluster 9 at $20 \mu\text{M}$ compound concentrations (**Figure 2b**). Inspection of individual electrophile profiles demonstrated corroboration with these overall trends, where electrophile clustering tended to migrate towards the gross injury cluster 9 at higher compound concentrations (**Figure 2c**). Most TEs did not produce the gross injury phenotype until concentrations in great excess of their expected EC_{50} values. These data show that both NSEs and TEs can produce CP phenotypes

associated with cellular injury, and that cellular injury phenotypes may help to identify highly reactive compounds including TEs with off-target toxicities.

Quality of KAT inhibitors are distinguishable by cell painting

The utility of certain compound classes, including lysine acetyltransferases (KATs), has recently been questioned²⁸⁻³¹. KATs are crucial components of eukaryotic DNA repair and nucleosome assembly, and aberrancies in histone acetylation and KAT function have been implicated in human pathologies including many cancers^{32,33}. Numerous small-molecule KAT inhibitors have been reported³⁴, but many of these “historical” KAT inhibitors (hKATIs) are enriched for nonspecific electrophilicity, aggregation, suboptimal potency and selectivity, and cytotoxicity³¹. However, highly potent and specific “next-generation” KAT inhibitors (ngKATIs) have now been reported, including the KAT3 inhibitor A-485 (**468**) and the KAT6 inhibitors WM-8014 (**470**) and WM-1119 (**471**)³⁵⁻³⁷. Given our previous experiences characterizing hKATIs for assay interference and their association with nonspecific activity, we sought to determine if differences in probe quality could be distinguished by profiling the ngKATIs **468-472** and hKATIs **473-501** using CP.

We first profiled the ngKATIs **468-472** for the cell-free liabilities characteristic of many hKATIs. In contrast to hKATIs, **468-472** showed acceptable profiles for potency, selectivity, reproducibility, colloidal aggregation, redox cycling, nonspecific thiol reactivity, chemical instability, light absorption, fluorescence, and quenching (**Supplementary Figures 4, 5; Supplementary Notes**). Furthermore, **468-472** were nontoxic and decreased cellular H3K27ac levels as expected in MCF7 and HEK293T cells (**Supplementary Figure 3**). By contrast, the interference compounds rottlerin (**478**) and plumbagin (**486**) also decreased cellular H3K27ac levels, but in addition reduced total cellular KAT3B (p300) levels. These data confirm the

reported on-target activities of **468-472** and indicate that they are unlikely to exhibit common assay interference modes.

The two KAT inhibitor categories produced distinct CP morphologies. Whereas the ngKATIs **468-472** were CP-inactive and had no effect on cell number, many hKATIs were active and strongly reduced cell numbers in CP (**Figure 3a**). More specifically, most hKATIs resulted in significantly increased activity (19/26, 73%) and decreased cell numbers (14/26, 54%) at 20 μ M. The ngKATIs occupied different PCA feature-space from most hKATIs, with the summary morphological fingerprints being essentially null for ngKATIs while the hKATIs mirrored cluster 9 (**Figure 3b**). Many hKATIs (6/26, 23%) produced the gross injury phenotype (cluster 9) at 20 μ M, and even more so at 80 μ M (10/17, 59%); a notable subset of hKATIs (9/26, 35%) produced the genotoxic phenotype (cluster 6) at 20 μ M. Inspection of individual KAT inhibitor profiles agreed with these overall observations, with the NSEs L002 (**481**) and NU-9056 (**490**) producing gross injury phenotypes at concentrations similar to other NSEs (**Figure 3c**). The prototypical aggregators anacardic acid (**487**) and MG149 (**493**) showed abrupt and concomitant increases in CP activity and decreased cell numbers near their approximate critical aggregation concentrations (CACs). Notably, many hKATIs were profiled at higher compound concentrations based on their reported cellular potencies.

Interestingly, histone acetylation status and CP morphologies were not correlated based on profiling cellular acetylated histones and KAT3B levels under conditions mimicking the CP assay (**Supplementary Figure 6**). These observations are consistent with previous reports that in certain prostate and hematologic cancer cell lines, cellular histone acetylation levels do not necessarily correlate with anti-proliferative effects³⁵. These data illustrate the subtle but important point that quality, on-target probes do not necessarily produce detectable CP

phenotypes, whereas nonspecific compounds can generate significant CP phenotypes. Robust phenotypes for processes like chromatin remodeling may require longer compound treatment times not amenable to standard CP conditions. Overall, the CP and interference profiling data support the use of ngKATIs **468-472** as quality epigenetic probes. Other ngKATIs likely behave similarly, given some shared chemical scaffolds and the lack of red-flag interference chemotypes^{38,39}.

Cellular health and cell painting compound profiles

We next sought to characterize the connection between CP-detected cellular injury-based phenotypes and more specific cellular health readouts by multiplexed live-cell imaging under CP-like conditions. The CP activities and relative cell numbers of 254 profiled compounds were correlated with culture confluence (phase contrast), caspase-3/7 activation (GFP channel, fluorogenic caspase 3/7 substrate), and cell viability (RFP channel, CytoTox dye which marks compromised membrane integrity) by live-cell imaging (**Figure 4a**). Compounds with the most pronounced changes in cell confluence, caspase 3/7 activation, and compromised membrane integrities were found in PCA clusters 7-9 (**Figures 4a, 4b**). Similar patterns occurred when analyzed by compound category, with hKATIs, MLI-HC, and NSEs exhibiting cellular damage profiles in live-cell imaging, whereas their respective ngKATI, MLI-NC, and NSE-IA counterparts were largely inert (**Figure 4b**). Individual compound profiles agreed with these overall observations, where adverse changes in cellular health biomarkers generally increased in magnitude and decreased in time-to-onset with higher compound concentrations (**Figure 4c**).

Live-cell imaging does not include washing steps prior to image acquisition and can potentially enrich for compounds acting by technology-related interferences like compound auto-fluorescence. Indeed, reagent-free counter-screens identified several auto-fluorescent compounds that were excluded from analyses (**Supplementary Figure 7**).

Given the importance of electrophilic and oxidative stress on cellular health, we profiled 99 select compounds at several concentrations to characterize the relationships between intracellular glutathione levels under CP-like conditions. The ngKATIs did not grossly perturb glutathione homeostasis, whereas many hKATIs (10/26, 38%), TEs (10/13, 77%), NSEs (12/15, 80%), and cellular injury compounds (14/26, 54%) lowered the GSH:GSSG ratio at 20 μ M where most of these compounds were also active in CP (**Figure 4d**). Together, these data further demonstrate that CP activity is susceptible to various mechanisms of compound-mediated cellular injury and can be used to refine our understanding of undesirable compounds.

Time-dependence of cellular injury morphologies

While most analyses focused on 24-h treatment times, we also profiled a subset of 397 compounds after 48-h incubation. We found a strong correlation between compound treatments with strong CP signals (**Figure 5a**). The individual CP clusters deriving from 24- and 48-h compound treatments were also correlated (**Figure 5b**). Comparing the unsupervised clustering of compounds at 24 and 48 h evinced general agreement (entanglement = 0.76; **Figure 5c**). Inspection of individual compound profiles supported these trends, with most compounds exhibiting similar cell numbers and bioactivities at 24- and 48-h treatment times (**Figure 5d**). These data suggest that many grossly cytotoxic compounds can produce detectable CP morphological changes by 24 h of treatment.

Proposed cellular nuisance control compounds

While it may be tempting to discard compounds that result in low cell numbers, one may unnecessarily eliminate potentially useful bioactive compounds from consideration (e.g., novel and potent anti-neoplastics). In cellular assays, the causative factors for phenotypes are not known *a priori* and require follow-up experiments^{3,40}. Focused chemical libraries composed of

bioactive reference compounds can be highly useful for characterizing cellular readouts⁴¹. Interference characterization is standard in clinical assay validation, and some industrial screening centers even utilize “informer sets” composed of nuisance and cytotoxic chemical matter^{42,43}.

Based on our data and cumulative experience with HTS, we propose an informer set of control compounds to model cell injury phenotypes in HCS and other phenotypic assays including mechanism-based and nonspecific modes of gross cellular injury (**Figure 6**). This set would ideally include multiple concentrations of each compound (i.e., nM to μ M), focused active and inactive chemical analogs (if available), and multiple chemotypes for each cell injury cluster (especially for cluster 9). Such focused redundancy can mitigate compound-specific effects and assess experimental imprecision^{44,45}. Such a proposed set could be adapted to a single 384-well microplate in qHTS format and should only represent an incremental cost in the context of larger-scale campaigns, especially if repeatedly used. This set would ideally be used in parallel with an informer set composed of FDA-approved drugs and high-quality chemical probes to assess for overlapping phenotypes⁴¹.

Discussion

Here we provide a set of nuisance and cytotoxic compounds of various mechanisms, a dataset documenting their morphological impacts, and a strategy for using them as landmarks alongside novel compounds of interest, or even for assessing an entire compound library. There is a growing interest in phenotypic assays for drug discovery and chemical biology due to their purported potential for improved *in vivo* and clinical translation^{40,46}. Phenotypic and high-content assays such as CP are attractive, target-agnostic approaches for biological annotation of compounds. However, active compounds in cellular assays can act by on- or off-target effects, meaning that without detailed follow-up experiments, readouts are essentially “black boxes”⁴⁷.

As a result, a significant obstacle in cellular assays are bioactive compounds that act *via* undesirable MoAs like cellular injury. Since complex phenotypes are difficult to predict *a priori*, one practical solution is to include known reference compounds.

To test this solution, we profiled 218 prototypical cytotoxic and nuisance compounds in qHTS format, using CP and companion cellular health assays, to characterize the relationships more systematically between morphology and cellular injury. Targeted and nonspecific electrophiles, along with historical and next-generation KAT inhibitors, served as important case studies. Several important trends emerged: (1) there is a clear relationship between many types of cellular injury and CP activity, (2) nonspecific and suboptimal probes such as hKATIs can produce profound CP phenotypes, (3) compound-mediated cellular damage (e.g., tubulin poisons, genotoxins) can produce robust CP phenotypes, and (4) compound concentration is a key modifier of cellular injury phenotypes such as NSEs, aggregators, and surfactants. The diversity of compounds in cluster 9 (often at high concentrations) may be partially explained by the proposed “cytotoxicity burst” phenomenon whereby compounds are thought to activate multiple stress responses rather than a singular molecular target^{48,49}. The clear association between CP activity and cellular damage suggests active compounds should be subjected to cellular health profiling.

This *Resource* expands upon existing open-source CP datasets due to its concentration-response format, time-course data, accompanying cellular health profiling data, and the intentional profiling of prototypical cellular injury compounds. The large volumes of data generated by high-content assays is a practical barrier that hinders reproducibility and scientific exchange in the field⁵⁰. To address this barrier, the entire 11 TB of raw images from this study (including all solvent controls), representing 1.04 million images in total, and the associated metadata are available *via* the open-source Image Data Resource (idr.openmicroscopy.org)⁵¹.

This *Resource* should enhance compound prioritization in complex cellular assays. Potential uses for this dataset include HCS and image-processing method development, MoA studies, informer set design, and compound triage^{52,53}. These data can be re-analyzed by alternative methods such as focusing on individual features or more complex analyses such as the point-of-departure metric^{20,54}.

Compounds may induce cell line-dependent phenotypes, as well as dependency on other experimental factors including treatment time, compound concentration, and culture media composition^{55,56}. Although we only profiled one cell line, this approach is likely generalizable to other biological systems. Supporting evidence includes: (1) the similar behaviors of hKATIs and prototypical interference compounds in MCF7, HEK293, and U-2 OS cells; (2) the profiled compounds were chosen based on activities unrelated to U-2 OS cells; and (3) the biological targets of these cellular injury compounds tend to be common amongst human cell lines. Our findings are complementary to but consistent with previous reports, including the robust phenotypes of cytoskeletal poisons, genotoxins, and other classes of cellular injury compounds^{13,45,55-58}. Furthermore, reference compounds can show similar phenotypes across different cell lines in HCS assays^{20,59-61}. Notably, our findings also mirror a profiling effort that combined gene expression and cell death profiles, which found compound clusters consisting of microtubule modulators, electrophiles, and genotoxins⁶².

Lastly, we propose a framework for constructing cellular injury informer sets applicable beyond CP, from alternative high-content morphology assays to orthogonal cellular assay technologies like gene-expression profiling and metabolomics. This set could have several applications in cellular assays. During the assay development and optimization phase, such a set could guide the choice of experimental conditions to minimize the selection of unwanted MoAs such as NSEs. During the screening phase, such a set could guide compound triage and follow-up

experiments, especially if new compounds share phenotypes with unwanted MoAs. Used in parallel with screening, such a set could facilitate real-time compound evaluation of high-risk chemical matter, and potentially reduce the necessity of certain follow-up counter-screens. In terms of practical use, compounds that produce similar phenotypes as cellular injury compounds can be prioritized (i.e., if assaying for novel or mechanism-based cytotoxins) or triaged (i.e., de-prioritizing tubulin or mitochondrial poisons). In one study, compounds profiled with the L1000 transcriptome profiling assay and CP, cytotoxic compounds produced robust signatures in both techniques⁴⁵. Nuisance and cellular injury compounds will likely show some assay-dependent effects, which further supports the value of repeatedly using an informer set. Future iterations focused on cellular injury could include MoAs not profiled, such as chelation, metal poisoning, and lysosomotropic agents. Future work could also characterize the effects of compound technology-related interferences (“artifacts”) such as auto-fluorescent or quenching compounds^{63,64}. We envision that collaboration between academic, industry, and government groups performing phenotypic screening can enhance our proposed informer set by nominating additional compounds and performing additional validation in orthogonal phenotyping assays and biological systems⁶⁵.

Online materials and methods

Compounds and reagents

Sources of KAT inhibitors are listed (**Supplementary Table 1**). Additional compounds were obtained from commercial vendors and the Broad Institute chemical screening library. Test compounds were typically prepared as 10 μ M stock solutions dissolved in neat DMSO and stored under vacuum seals in either -20 °C or a light-shielded desiccation chamber at RT. All were subjected to internal quality control⁶⁶; most demonstrated > 90% purity and detection of an expected parent ion by UPLC-MS (**Supplementary Data 1**).

Cell lines

HEK293T cells were gifted from Dr. Sam Benchimol (York University); MCF7 and U-2 OS cells were obtained directly from ATTC (cat # HTB-22 and HTB-96, respectively). HEK293T and MCF7 cells were used to remain consistent with our previous report³¹. U-2 OS cells were used for CP because they form monolayers highly amenable to single-plane high-content imaging and have been profiled extensively at several institutions^{7,14}. U-2 OS cells do not contain significant genetic perturbations in KAT3 (**Supplementary Notes**). Cell-line identities were confirmed by short tandem repeat profiling (ATCC Cell Line Authentication Service), and *Mycoplasma* contamination was assessed with the MycoAlert PLUS *Mycoplasma* Detection Kit (Lonza, cat # LT07-701).

Cell painting

Cell painting (CP) was adapted from previous reports^{6,7}. New U-2 OS cells were purchased directly from ATCC for each CP experiment and used within the first ten passage numbers. U-2 OS cells were cultured in DMEM (high glucose, GlutaMAX, HEPES; Thermo Fisher, cat # 10564011) supplemented with 10% fetal bovine serum (FBS, v/v; Gibco, cat # 26140079), penicillin (100 μ U mL⁻¹), and streptomycin (100 μ g mL⁻¹), and maintained in a 37 °C, 5% CO₂

humidified incubator. Cells were dispensed by Thermo Multidrop into 384-well clear-bottom imaging plates (CellCarrier-384 Ultra; PerkinElmer, cat # 6057300). Each well contained approximately 750 (48 h treatment) or 1,500 (24 h treatment) cells in 50 μ L complete media. Cell counts were determined by Countess II automated cell counter (Thermo Fisher) using 0.4% trypan blue solution (Thermo Fisher, cat # T10282). Seeded microplates were incubated for 24 h at 37 °C, then treated with compounds or vehicle controls dispensed by pin tool transfer via CyBi-Well robot. Compounds were typically tested at six concentrations with 2-fold serial dilutions, ranging from 20 μ M to 625 nM final compound concentrations. Each plate contained four positive control compounds (**1-4**; colchicine, nocodazole, radicicol, wortmannin) at six concentrations each and 116 vehicle control wells (**Supplementary Notes**). Following the addition of compounds, cells were incubated at 37 °C for either 24 or 48 h.

A 1 mM DMSO solution of MitoTracker Deep Red FM (Invitrogen, cat # M22426) was added to pre-warmed complete media to make staining solution 1 (SS1) with final concentrations 500 nM MitoTracker. A 1 mg mL⁻¹ solution in 0.1 M aqueous sodium bicarbonate of concanavalin A-Alexa Fluor 488 conjugate (Invitrogen, cat # C11252), a 200 U mL⁻¹ methanol solution of phalloidin-Alexa Fluor 568 conjugate (Invitrogen, cat # A12380), a 1 mg mL⁻¹ dH₂O solution of wheat germ agglutinin (WGA)-Alexa Fluor 555 conjugate (Invitrogen, cat # W32464), a 16.2 mM aqueous solution of Hoechst 33342 (Invitrogen, cat # H3570), and a 5 mM DMSO solution of SYTO 14 green fluorescent nucleic acid stain (Invitrogen, cat # S7576) were combined in 1X HBSS (prepared from 10X solution, Thermo Fisher, cat # 14065-056; filtered) supplemented with 1% bovine serum albumin (BSA; m/v) to make staining solution 2 (SS2) with final concentrations 100 μ g mL⁻¹ concanavalin A, 0.5 U mL⁻¹ phalloidin, 60 μ g mL⁻¹ WGA, 8.1 μ M Hoechst, and 3 μ M SYTO 14.

Compound-treated cells were prepared for fixation and staining by first removing 40 μ L of media from each microplate well using a BioTek ELK405 automated plate washer. To each well, 30 μ L of SS1 were dispensed by Multidrop, followed by incubation for 30 min at 37 °C. Cells were then fixed by dispensing 10 μ L per well of 16% aqueous paraformaldehyde *via* Multidrop, followed by incubation for 20 min at RT. Next, wells were washed with 70 μ L 1X HBSS. Cells were then permeabilized by adding 30 μ L per well of 0.1% Triton X-100 (v/v) in 1X HBSS and incubated for 15 min at RT. Wells were then washed with 70 μ L 1X HBSS. Permeabilized cells were then stained by dispensing 30 μ L SS2 per well *via* Multidrop followed by incubation at RT for 30 min. Wells were washed with 70 μ L 1X HBSS without a final aspiration, then the plates were manually sealed with adhesive foil for subsequent imaging.

Cells were imaged using an Opera Phenix High-Content Screening System (PerkinElmer) in wide-field mode with a water-immersion 20X objective and five excitation/emission laser wavelengths: 405/435-480 (Hoechst), 488/500-550 (concanavalin A), 488/570-630 (SYTO 14), 561/570-630 (phalloidin and WGA), and 640/650-760 (Mito-Tracker) nm. Photobleaching of low-intensity dyes was mitigated by imaging in the following channel order: MitoTracker, WGA, phalloidin, SYTO 14, concanavalin A, and Hoechst 33342. Nine sites were imaged per well in a 3 x 3 array with laser-based autofocus on the first site per well. Concentration-response data are mean \pm SD from four intra-run technical replicates each performed on separate microplates.

Cell painting analyses

Morphological features were extracted from the raw CP images using a freely available CellProfiler software pipeline provided by the Broad Institute Imaging Platform^{7,67}. Images were corrected for uneven illumination, then CellProfiler (version 2.1.1) was used to locate and segment cells into nuclei and cytoplasm, after which the size, shape, texture, intensity, local density, and radial distributions were measured for nuclei, cytoplasm, and entire cells. To obtain

profiles for each compound, the morphological features of compound-treated cells were calculated for each well field, then averaged per well, and then normalized by calculating robust z-score-like values based on the population of individual DMSO-treated cells found on the same plate.

To determine the compound activities (“activity scores”), Mahalanobis distances of each compound profile were calculated from vehicle-treated well profiles⁶⁸. The profiles for all replicates of a compound were first combined with the corresponding DMSO-control wells into a matrix of dimensions $m \times n$, where the rows m represent the individual wells and the columns n represent the profiling features. PCA was performed on this matrix to obtain a new matrix P with the principal components as the columns. For each of these matrices, the first q principal components were taken that could explain $\geq 90\%$ of the variance. This matrix P was separated into treatment and control matrices and for each part a covariance matrix was calculated. Each of the two covariance matrices (treatment and control) was weighted by the number of samples in each matrix, and the sum of the resulting matrices was used to calculate the Mahalanobis distance. The R *cytominer* package was used to reduce the number of redundant features by removing those which were highly correlated. After processing, 372 non-redundant cellular features were used in the subsequent analyses.

The principal component analyses were performed using the *R stats* package (version 3.6.1) using non-aggregated treatment profiles (i.e., compounds, concentrations, and replicates separate) with scaling and without centering. These principal components were used for all PCA plots; for PCA plots containing only a subset of the data or using aggregated data, points were transformed into this space using the loadings of these principal components. Unsupervised hierarchical clustering was performed using the *R stats* package (version 3.6.1), using the values $[1 - \text{Pearson correlation}]$ as the pairwise distances between each treatment condition and

Ward's method (minimal increase of sum-of-squares). Entanglement was analyzed by comparing hierarchical clustering of the 24 and 48 h compound treatment duration CP data by Ward's method using the *R dendextend* package (version 1.13.2). To generate "dot plots," the values for the activity scores were averaged across all categories falling under a particular cluster (obtained from hierarchical clustering). To calculate the similarity of historical MLI CP data to the observed cellular injury phenotypes obtained from hierarchical clustering, only features belonging to the reduced feature set and shared between the historical data and this study were considered. Phenotypes are calculated as the average signature of each cluster, where the average value for each feature across all cluster members are taken, and the vector comprising these average values is used as the cluster phenotype (see also **Supplementary Figure 2**).

Live-cell imaging

U-2 OS cells were cultured similarly to the CP protocol but were modified for seeding density (750 cells in 25 μ L media per well), microplate (384-well, tissue culture-treated, black polystyrene, clear flat-bottom microplates; Corning, cat # 3764BC), and media (F-12K, ATCC, cat # 30-2004; supplemented with 10% FBS, 100 \square U mL⁻¹ penicillin, and 100 \square μ g mL⁻¹ streptomycin). This media was selected because it reduced background fluorescence in the GFP channel due to riboflavin⁶⁹. Seeded microplates were then incubated for 24 h at 37 $^{\circ}$ C, followed by the addition of sterile-filtered 25 μ L media to each well containing live-cell imaging reagents (Incucyte Cytotox Red Reagent, final concentration 250 nM, cat # 4632; Incucyte Caspase 3/7 Green Reagent, final concentration 5 μ M, cat # 4440). Cells were then immediately treated with 100 nL of compounds or vehicle controls dispensed by pin tool transfer *via* CyBi-Well Vario with a constant DMSO concentration of 0.2% (v/v). Most compounds were tested at three concentrations (20, 10, and 5 μ M final concentrations). Each microplate contained reagent-free control wells to correct for cellular auto-fluorescence. Following compound

addition, cells were incubated at 37 °C for 60 h and imaged every 4 h with an Incucyte S3 Live-Cell Analysis System (Essen Biosciences) utilizing 10X objective and 300 and 400 ms GFP and RFP channel acquisition times, respectively. Live-cell images were processed in Incucyte Analysis Software (Essen Biosciences) using top-hat background correction. Data are mean \pm SD from three intra-run technical replicates each performed on separate microplates. To analyze compounds tested in concentration-response format, area under the curve (AUC) was calculated as described previously⁷⁰.

Intracellular glutathione quantification

U-2 OS cells were cultured similarly to the aforementioned CP protocol, except for seeding density (750 cells in 25 μ L media per well) and microplate (384-well, tissue culture-treated, low-volume, white polystyrene, flat-bottom microplates; Corning, cat # 8867BC). Seeded microplates were then incubated for 24 h at 37 °C, then treated with 100 nL compounds or vehicle controls dispensed by pin tool transfer via CyBi-Well Vario with a constant DMSO concentration of 0.4% (v/v). Most compounds were tested at three concentrations (20, 10, and 5 μ M final concentrations). Following the addition of compounds, cells were incubated at 37 °C for 24 h. Each microplate contained triplicate 10-point GSH standards (6.4 μ M to 13 nM by 2-fold serial dilutions) for quantifying GSH. After compound treatment, total intracellular glutathione (reduced, GSH and oxidized, GSSG) concentrations and oxidized glutathione (GSSG) were quantified in parallel on separate microplates with the GSH/GSSG-Glo kit (Promega, cat # V6611) per manufacturer protocol, except that all reagents were diluted three-fold in PBS. Cell viability was quantified in parallel on separate microplates by Cell Titer Glo (Promega, cat # G7570) per manufacturer protocol. Luminescence was measured on an Envision 2105 plate reader (PerkinElmer) with 400 ms acquisition times. Data were corrected for background luminescence using cell-free control wells and for row/column effects by uniformity plates. Data are from five intra-run technical replicates each performed on separate microplates.

Interference profiling of next-generation KAT inhibitors

Biochemical KAT selectivity. ngKATIs were tested for biochemical selectivity versus six KATs.

Assay conditions were as follows: KAT2A (hGCN5, 497-662 aa), 1 nM enzyme, 10 μ M biotin-H3 1-25, 2.5 μ M [3 H]-acetyl-CoA; KAT3B (P300, 1195-1662 aa), 2 nM enzyme, 5 μ M biotin-H3 1-25, 2.5 μ M [3 H]-acetyl-CoA; KAT1 (HAT1, 20-341 aa), 1 nM enzyme, 1 μ M biotin-H4 1-24, 5 μ M [3 H]-acetyl-CoA; KAT6A (MOZ/MYST3, 472-793 aa), 10 nM enzyme, 10 μ M biotin-H4 1-24, 5 μ M [3 H]-acetyl-CoA; KAT5 (TIP60, 1-513 aa), 10 nM enzyme, 1 μ M biotin-H4 1-24, 0.25 μ M [3 H]-acetyl-CoA; KAT8 (HMOF/MYST1, 2-458 aa), 20 nM enzyme, 10 μ M biotin-H4 1-24, 1 μ M [3 H]-acetyl-CoA. For KAT3B testing, buffer conditions were 100 mM HEPES, pH 8.0, 2 mM DTT, 100 mM KCl, 80 μ M EDTA, 40 μ g mL⁻¹ BSA (m/v), 0.01% Triton X-100 (v/v). For KAT1/3B/5/6A/8 testing, buffer conditions were 20 mM tris, pH 8.0, 5 mM DTT, 0.01% Triton X-100 (v/v). Reactions were performed at 23 °C for 20 min. Final DMSO concentration was constant at 2.0% (v/v). Percent activity represents acetylation relative to vehicle control reactions. Concentration responses were analyzed by nonlinear least-squares regression fits to a four-parameter logistic (“4PL”) equation. KAT profiling data are mean of two intra-run technical replicates. Concentration-response KAT6A data are mean \pm SD from three intra-run technical replicates.

Biochemical KAT3B activity. Inhibition of KAT3B acetyltransferase activity by ngKATIs was assessed by a separation-based assay⁷¹. Reactions consisted of buffer (50 mM HEPES, pH 7.5, 50 mM NaCl, 2 mM EDTA, 2 mM DTT, 0.05% Triton-X-100) with KAT3B (P300, 150 nM) and FITC-Ahx-RGKGGKGLGKGG [Ahx = 6-aminohexanoic acid] substrate (2 μ M) were plated in 384-well microplates and equilibrated at RT for 10 min in the presence or absence of inhibitor. Reactions were initiated by addition of acetyl-CoA (1 μ M final concentration) with 30 μ L final assay volume and quenched during steady-state kinetics (< 15% product accumulation) by

addition of 5 μ L of 0.5 M neutral hydroxylamine. Quenched reaction aliquots were then transferred to a PerkinElmer Lab-Chip EZ-Reader instrument for microfluidic electrophoresis and fluorometric analysis. Optimized separation conditions were downstream voltage -500 V, upstream voltage -2500 V, and pressure -1.5 psi. Percent conversion is calculated by ratiometric measurement of substrate/product peak heights, corrected for nonenzymatic background acetylation. Percent activity KAT3B represents acetylation relative to vehicle control. Concentration responses were analyzed by nonlinear least-squares regression fits to a 4PL equation. Data are mean \pm SD from three technical replicates.

ALARM NMR. ngKATIs were tested by ALARM NMR for protein thiol reactivity as previously described⁷². The human La antigen (aa 100–324, Δ T302N) was expressed in *Escherichia coli* Rosetta cells (Novagen) and cultured in M9 minimal media. The La antigen was labeled by adding ¹³C-labeled amino acid precursors ([3-¹³C]- α -ketobutyrate and [3,3'-¹³C]- α -ketoisovalerate sodium salts; Cambridge Isotope Laboratories) to culture medium 30 min before IPTG induction. Bacteria were harvested after induction at 25°C for 8 h, followed by lysis *via* French press. Labelled La antigen was purified by standard Ni-NTA bead purification. The La antigen product was dialyzed (25 mM sodium phosphate, pH 7.0, 5 mM DTT) in three 16 h cycles at 4°C with gentle stirring. Aliquots were flash-frozen in liquid N₂ and stored at -80°C until further use. Before use, hLa protein was reduced by incubating with 20 mM DTT at 37°C for 1 h, then dialyzed (25 mM sodium phosphate buffer, pH 7.0, no DTT) in three 16 h cycles at 4°C with constant nitrogen bubbling and with gentle stirring. The [¹H-¹³C]-HMQC spectra were acquired in 25 mM sodium phosphate buffer, pH 7.0, 10% D₂O (v/v; CIL) \pm 200 μ M test compounds \pm 20 mM non-deuterated DTT. Final concentration of DMSO was 4.0% (v/v). Reaction solutions were incubated at 37°C for 1 h and then 30°C for 15 h before obtaining spectra. Data were recorded at 310 K on a Bruker UltraShield

700 MHz NMR spectrometer equipped with a Bruker 1.7 mm TCI Cryoprobe and Bruker SampleJet autosampler. Samples were tested at 50 μ M protein concentrations using 16 scans, 2048 complex points in F2, and 80 points in F1 using standard protein [^1H - ^{13}C]-HMQC and water suppression pulse sequences. Sample tubes were inspected for gross compound precipitation. NMR data were analyzed in Bruker TopSpin (version 4.0.7). Reactions were normalized to DMSO controls. Nonreactive compounds were identified by the absence of chemical shifts or changes in peak intensities (^{13}C -methyl) \pm 20 mM DTT. Reactive compounds induced chemical shifts and decreases in peak intensities in certain diagnostic peaks in the absence of DTT.

Chemical stability and GSH adducts by UPLC-MS. Gross compound stability of ngKATIs was assessed by incubating parent compound (20 μ M final concentrations) in PBS, pH 7.4 at 37 $^{\circ}\text{C}$ for 4 and 24 h. Samples were spiked with fluconazole internal standard (10 μ M final concentration, Cerilliant), then diluted with equivolumetric amounts of MeOH to mitigate ion suppression by PBS, then passed through 0.2 μ m pore size syringe filters. Samples were also compared to otherwise identical samples containing parent compounds incubated in neat MeOH instead of buffer. Samples were analyzed using a Waters ACQUITY UPLC system using a BEH C18 2.1 \times 50 mm column. Samples were injected by an autosampler in 5 μ L sample volumes. The flow rate was 0.250 mL min^{-1} with a standard gradient starting at 95% Solution A (950 mL H_2O , 50 mL MeCN, 1 mL formic acid) and ending with 100% Solution B (1000 mL MeCN plus 1 mL formic acid) over 2.0 min. The samples were monitored simultaneously by a PDA detector and a ZQ mass spectrometer (electrospray, positive and negative modes). Chromatograms and mass spectra were qualitatively analyzed for the formation of new peaks and/or loss of parent signal relative to internal standard. To detect GSH adducts, test compounds (20 μ M final concentrations; 1 μ eq) and reduced L-glutathione (20 μ eq) were incubated in PBS, pH 7.4 at 37 $^{\circ}\text{C}$ for 4 h. Samples were prepared identically to

the chemical stability studies, but the internal standard was omitted to avoid possible interference with detecting potential compound-GSH adducts. Chromatograms and mass spectra were qualitatively analyzed for characteristic compound-GSH adduct ions by examining the PDA chromatograms for new peaks and the ion chromatograms for loss of the GSH ion (e.g., 307 m/z). CPM (Sigma, catalog # C1484) was used as a positive GSH-reactive control compound. UPLC-MS data were analyzed in MestReNova (version 14.1.0-24037).

Fluorescence intensity thiol reactivity counter-screen. The ngKATIs were tested for non-proteinaceous thiol reactivity using adaptations of previous procedures^{2,73}. Thiol-free buffer (25 mM sodium phosphate, pH 7.0, 0.01% Tween-20 v/v) was dispensed in 10 μ L volumes into black polypropylene 384-well round-bottom microplates (Agilent, cat # 201290-100) *via* Multidrop. DMSO, 10 μ M *N*-ethyl maleimide (NEM, Sigma, cat # E1271), and 250 μ M BHQ-10 (carboxylic acid, Biosearch) were used as negative, positive reactivity, and positive light interference controls, respectively. Compounds and positive controls (NEM) were transferred to assay plates in 100 nL volumes by pin-tool *via* CyBi-Well Vario 384/60 (CyBio). Final DMSO concentration was constant at 2.5% (v/v). GSH, CoA, and NAC were freshly prepared as 2 μ M solutions in buffer (25 mM sodium phosphate, pH 7.0, 0.01% Tween-20 v/v) and dispensed to the aforementioned microplates in 10 μ L volumes *via* Multidrop (1 μ M thiol, final concentration). After thermal sealing (Agilent PlateLoc), microplates were incubated for 90 min at 37 °C in an incubator oven, followed by the addition *via* Multidrop of 10 μ L solution containing 12 μ M thiol-reactive probe CPM (Sigma, cat # C1484) prepared in 1:1 DMSO:water. After incubation at RT for 5 min, thiol reactivity was quantified by measuring fluorescence intensity (λ_{ex} 405 nm, λ_{em} 530 nm) on a SpectraMax M3 plate reader (Molecular Devices; PMT automatic gain, 10 flashes per well). Compounds signals were background-corrected by subtracting the mean negative-

control plate control signals. Data are mean \pm SD from three intra-run technical replicates performed on the same microplate.

AmpC aggregation counter-screen. KAT inhibitors were assessed for aggregation using a modified AmpC β -lactamase counter-screen⁷⁴. Recombinant *E. coli* AmpC was obtained from Rosetta cells using a published protocol⁷⁵. The purified protein product was > 95% pure by SDS-PAGE analyses and migrated identically to an AmpC standard (Shoichet lab). The enzymatic assay was performed in 50 mM sodium phosphate, pH 7.0 in clear cyclic olefin copolymer 384-well microplates (Aurora, cat # 3030-00330) in 75 μ L reaction volumes. Compounds were tested in triplicate at 4, 11, 33, and 100 μ M final concentrations in buffer \pm freshly-added 0.01% Triton X-100 (v/v). Final concentration of DMSO was 1.0% (v/v). Compounds were incubated with 5 nM AmpC in 73.5 μ L reaction buffer for 5 min at RT, followed by the addition of 1.5 μ L of nitrocefin substrate (Cayman, cat # 15424) dissolved in DMSO (100 μ M initial substrate concentration). Reaction solutions were gently mixed by multichannel pipette. Reaction progress was continuously monitored by absorbance at 482 nm for 5 min at RT on a SpectraMax M3 plate reader, and percent activity was calculated from reaction rates (slope). Percent activity was normalized to DMSO-only controls after background subtraction with an enzyme-free reaction. Avibactam (Cayman, cat # 22825), non-aggregation AmpC positive control. Statistical significance ($p < 0.05$) was evaluated without assuming consistent SD using two-tailed Student's t-test and the Holm-Sidak method to control for multiple comparisons. Data are mean \pm SD from four intra-run technical replicates.

MDH aggregation counter-screen. KAT inhibitors were also assessed for aggregation using a modified malate dehydrogenase counter-screen⁷⁶. The enzymatic assay was performed in 50 mM sodium phosphate, pH 7.0 in clear cyclic olefin copolymer 384-well microplates

(Aurora, cat # 3030-00330) in 75 μ L reaction volumes. Compounds were tested in triplicate at 100 μ M final concentrations in buffer \pm freshly added 0.01% Triton X-100 (v/v). Final concentration of DMSO was 1.0% (v/v). Compounds were incubated with 1 μ M porcine heart MDH (EMD Millipore, cat # 442610) in 73.5 μ L reaction buffer for 5 min at RT, followed by the addition of 1.5 μ L of substrate (200 μ M oxaloacetate and 200 μ M NADH final concentrations; derived from fresh 20 mM stocks in 50 mM sodium phosphate, pH 7.0) and then gentle mixing with multichannel pipette. Reaction progress was continuously monitored by absorbance at 340 nm for 5 min at RT on a SpectraMax M3 plate reader, and percent activity was calculated from reaction rates (slope) and normalized to DMSO-only controls. Statistical significance ($p < 0.05$) was evaluated without assuming consistent standard deviation using two-tailed Student's t-test and the Holm-Sidak method to control for multiple comparisons. Data are mean \pm SD from four to eight intra-run technical replicates.

DLS aggregation counter-screen. Dynamic light scattering was performed as previously described⁷⁶. DMSO stocks of KAT inhibitors were diluted in filtered 50 mM potassium phosphate, pH 7.0, final concentration 1% DMSO (v/v). Light scattering was recorded using a DynaPro Plate Reader II system (Wyatt Technology) with a 60-mW laser at 830 nm, 158° detection angle, and automatically adjusted laser power. Notably this instrument is configured with a larger-width laser beam width optimized for detecting large colloidal particles (BK Shoichet lab, USCF). Data were acquired and processed by Dynamics software (Wyatt). Cut-off for colloidal aggregation is 10^6 counts sec^{-1} . Data are mean \pm SD from two or three intra-run technical replicates performed on the same microplate.

Redox activity counter-screen. ngKATIs were assessed for hydrogen peroxide production using a horseradish peroxidase-phenol red counter-screen⁷⁷. Testing was performed in buffer

(50 mM tris, pH 7.0) plus 0.01% Triton X-100 (v/v) in clear cyclic olefin copolymer 384-well microplates (Aurora, cat # 3030-00330) in 60 μ L reaction volumes. Compounds were tested at 250 μ M final concentrations. Final concentration of DMSO was constant at 2.5% (v/v). Compounds were incubated in 40 μ L reaction buffer (\pm 1 mM DTT final concentration) for 20 min, followed by the addition of 20 μ L solution containing phenol red and horseradish peroxidase (Sigma) dissolved in reaction buffer. Final concentrations of phenol red and horseradish peroxidase were 280 μ M and 60 μ g mL⁻¹, respectively. The reaction solution was allowed to incubate for 20 min at RT, followed by the addition of 10 μ L of 1 M sodium hydroxide *via* multichannel pipette to quench the reaction. After 10 min incubation at RT, hydrogen peroxide was quantified by measuring absorbance at 610 nm on a SpectraMax M3 plate reader. DMSO and 100 μ M hydrogen peroxide were used as negative and positive controls, respectively. NSC-663284 (**479**; Cayman, cat # 13303) and 4-amino-1-naphthol HCl (**67**; Oakwood Chemical, cat # 013411) were used as positive compound controls^{78,79}. Data are mean \pm SD from three intra-run technical replicates performed on the same microplate.

Light absorbance counter-screen. ngKATIs were assessed for light absorption between 200 and 750 nm at 100 μ M final compound concentrations in filtered sodium phosphate buffer (50 mM sodium phosphate, pH 7.0). Final concentration of DMSO were constant at 1.0% (v/v). Compounds were allowed to incubate at RT in buffer for 10 min in UV-transparent half-area 96-well microplates (Corning, cat # 3679). Absorbance spectra were then obtained using a SpectraMax M3 microplate reader at 25 °C using buffer plus DMSO as blank.

Auto-fluorescence counter-screen. ngKATIs were assessed for auto-fluorescence using an adaption of published procedures⁸⁰. Briefly, fluorophore standards consisted of AlexaFluor 350 (carboxylic acid, Invitrogen, cat # A33076), AlexaFluor 488 (carboxylic acid, Invitrogen, cat #

A33077), AlexaFluor 647 (carboxylic acid, Invitrogen, cat # A33084), Texas Red (succinimidyl ester, Invitrogen, cat # T6134), fluorescein (Sigma, cat # F2456), and resorufin (Sigma, cat # 424455). Test compounds were tested in triplicate at six final concentrations (32 nM to 100 μM via five-fold serial dilutions). Fluorophores were tested in triplicate at five to seven final concentrations (0.5 nM to 3 μM). Final concentration of DMSO was constant at 2.0% (v/v). Compounds and fluorophore standards were prepared as serial dilutions from 10 mM DMSO stock solutions, then transferred to 384-well non-binding surface black polystyrene microplates (Corning, cat # 3575) *via* multichannel pipette. Plate arrangements were purposefully designed to minimize optical crosstalk by the various fluorophores and test compounds. All measurements were performed at 25 °C in 60 μL of 50 mM tris, pH 8.0, dispensed into microplates *via* multichannel pipette. Compounds were shaken for 2 min on a plate shaker, centrifuged briefly for 1 min at 500×g, then allowed to incubate at RT in light-reduced conditions for 10 min before measuring fluorescence intensity on a SpectraMax i3x plate reader under reduced lighting. Instrument settings: excitation filter wavelength (nm), emission filter wavelength (nm) with bandwidth filter widths in nm denoted in parentheses: AlexaFluor 350, 340 (15), 450 (15); fluorescein, 480 (15), 540 (25); AlexaFluor 488, 480 (15), 540 (25); Resorufin, 525 (15), 598 (25); Texas Red, 547 (9), 618 (15); and AlexaFluor 647, 570 (9), 671 (15). Compound fluorescence intensity for fluorophores and test compounds was measured at each of the six fluorophore standard settings. Fluorophore standards present on each microplate were then used to construct normalized fluorescence concentration-responses (“fluorophore-equivalent concentrations”, FEC) by nonlinear regression with 1/Y weighting. Lower limits of quantification (LLOQ) had > 3:1 signal:noise ratio. Fluorescence intensities for each test compound were then converted to FECs. Calculated concentrations below the lower limits of quantification were scored as zero. Fluorophores prepared from independent dilutions as the calibrators were used as positive controls. Data are mean ± SD from three intra-run technical replicates performed on the same microplate.

Quenching counter-screen. ngKATIs were assessed for fluorescence quenching using adaptations of previously published procedures⁸⁰. Test compounds and individual fluorophore standards prepared separately in assay buffer were incubated together, and the fluorescence intensity of these compound-fluorophore mixtures was compared to vehicle controls. Compounds were tested in triplicate at six final concentrations (32 nM to 100 μM via five-fold serial dilutions) at a fixed 250 nM fluorophore final concentration. All measurements were performed in 50 mM Tris, pH 8.0 at 25 °C in 384-well black polystyrene microplates (Corning, cat # 3575) with 60 μL assay volumes. Compounds and fluorophore solutions were dispensed into microplates via multichannel pipette. Final concentration of DMSO was constant at 4.0% (v/v). Solutions were shaken for 2 min on a plate shaker, centrifuged briefly for 1 min at 500×g, then incubated at RT in light-reduced conditions for 10 min before measuring fluorescence intensity on a SpectraMax i3x plate reader using the filter settings for each fluorophore. BHQ-10 carboxylic acid (LGC Biosearch Technologies, cat # BHQ-10-5) was used as a positive fluorescence quenching control compound. Significant fluorescence quenching was defined as signal reduction > 25% of the corresponding fluorophore signal at any test compound concentration. Data are mean ± SD from three intra-run technical replicates performed on the same microplate.

Immortalized cell line histone acetylation assays. Select historical and next-generation KAT inhibitors were tested for their effects on cellular proliferation and H3K27ac levels in HEK293T and MCF7 cells as previously reported³¹. Cells were cultured in Dulbecco's Modified Eagle's Medium (DMEM) supplemented with 10% FBS (v/v; Winstent), penicillin (100 U mL⁻¹), and streptomycin (100 μg mL⁻¹). For cell growth analyses, cells were seeded in 96-well microplates, treated with the indicated compounds, and continuously monitored for 24 h using a live-cell Incucyte ZOOM imager (Essen Biosciences). Nuclei counts were determined using Vybrant

DyeCycle Green (Invitrogen, cat # V35004, dilution 1:5000). Data are mean \pm SD from three technical replicates performed on the same microplate.

For western blot analysis of H3K27ac, cells were treated for 24 h with compounds and lysed in ice-cold lysis buffer (20 mM tris-HCl, pH 8, 150 mM NaCl, 1 mM EDTA, 10 mM MgCl₂, 0.5% Triton X-100 (v/v), 12.5 U mL⁻¹ benzonase (Sigma, cat # E8263), complete EDTA-free protease inhibitor cocktail (Roche). After 3 min incubation, SDS was added to final 1% concentration (w/v). Total cell lysates were resolved using 4-12% bis-tris protein gels (Invitrogen) with MOPS buffer (Invitrogen) and transferred onto PVDF membranes (Millipore) in tris-glycine transfer buffer containing 10% MeOH (v/v) and 0.05% SDS (w/v). Membranes were blocked for 1 h in blocking buffer (5% milk in 0.1% Tween-20/PBS) and probed with the indicated primary antibodies overnight at 4 °C: H3K27ac (Cell Signaling Technologies, cat # 8173, dilution 1:1,000), H3 (Abcam, cat # 10799, dilution 1:1,000), and KAT3B (Bethyl, cat # A300-358A, dilution 1:2,000). The following secondary antibodies were used according to manufacturer instructions: goat anti-rabbit IgG (IRDye 800-conjugated, LI-COR, cat # 926-32211, dilution 1:5,000) and donkey anti-mouse IgG (IRDye 680-conjugated, LI-COR, cat # 926-68072, dilution 1:5,000). The signal was acquired on an Odyssey scanner (LI-COR) at 800 nm and 700 nm.

Western blots in U-2 OS cells were performed similarly as above. Cells were cultured in DMEM (Thermo Fisher, cat # 10564011) supplemented with 10% FBS (v/v; Sigma, cat # F6178), penicillin (100 U mL⁻¹), and streptomycin (100 µg mL⁻¹), and maintained in a 37 °C, 5% CO₂ humidified incubator. Prior to compound treatment, 240,000 U-2 OS cells were plated per well in the above media in 6-well plates. The subsequent day, select compounds dissolved in neat DMSO were added to each well to the listed final concentration. The final DMSO concentration was maintained constant at 0.2% (v/v). After 24 h treatment, cells were harvested in 4X SDS-

PAGE lysis buffer and boiled to denature. Cell lysates were separated on 16% tris-glycine gels (Thermo Fisher, cat # XP00165) for smaller proteins. For larger proteins, lysates were separated on 3-8% tris-acetate gels (Thermo Fisher, cat # EA03785). All proteins were transferred to membranes *via* iBlot (Thermo Fisher). For KAT3B, membranes were blocked in 5% milk-TBS for 1 h, and then probed for KAT3B (Bethyl, cat # A300-358A, dilution 1:10,000) overnight in 2.5% milk-TBST (2.5% milk in 0.05% Tween-20/TBS). GAPDH (CST, cat # 2118S, dilution 1:2,000) was also probed in 2.5% milk-TBST overnight at 4 °C. All other proteins were probed in 2.5% BSA-TBST (2.5% BSA in 0.1% Tween-20/TBS) overnight at 4 °C with the following dilutions: total H3 (Abcam, cat # AB1791, dilution 1:5,000); H3K14ac (Millipore, cat # 07-353, dilution 1:2,000); and H3K27ac (CST, cat # 8173, dilution 1:2,000). All blots were probed with an anti-rabbit HRP conjugated secondary antibody (CST, cat # 7074S, dilution 1:5,000) and washed with TBST (0.1% Tween-20/TBS) before visualization with enhanced chemiluminescence substrate.

Data analyses and figure preparation

All graphical data are expressed as mean \pm standard deviation (SD) unless stated otherwise. Graphing and statistical analyses were performed using Prism (GraphPad, version 8.4.2) or *R* (version 3.6.1). Final figures were prepared in Adobe Illustrator (version 25.0).

Data availability

The following data are deposited at Figshare ([10.6084/m9.figshare.20293992](https://doi.org/10.6084/m9.figshare.20293992)) and are available without restriction: (1) CP extracted features, (2) processed live-cell imaging data, (3) processed intracellular glutathione data, and (4) ALARM NMR spectra and UPLC-MS chromatograms for KAT inhibitors. The multi-terabyte collection of CP images, metadata, and associated CellProfiler object-level files are deposited at the Image Data Resource

(idr.openmicroscopy.org, accession number idr0133). All other relevant data are available from the authors without restriction.

Supplementary materials

Supplementary Information: File containing Supplementary Figures 1-6, Supplementary Notes, and Supplementary References (PDF). Supplementary Data 1: Key compound descriptors (SMILES, purity, annotations) for study compounds (XLSX).

Preprint status

This manuscript and supplementary materials have been uploaded to bioRxiv.

Acknowledgements

Authors acknowledge Hayarpi Torosyan for technical assistance with AmpC purification; Brian Shoichet (sponsored by NIH R35GM122481) for help with aggregation controls, Maria Alimova and Jean Santos for assistance with CP image acquisition; Ryan Babcock, Allison Hands, Charlotte Sandland, and Anita Vrcic for compound management; Broad Pattern team for assistance with data visualization; and Liz Fuller for laboratory management.

This study was supported by the Ono Pharma Breakthrough Science Initiative Award (to BKW). Authors acknowledge the following financial support: JLD (NIH NHLBI, T32-HL007627); BKH (National Science Foundation, DGE1144152 and DGE1745303); BEZ (NIH NIGMS, K99-GM124357); SDN (Harvard University's Graduate Prize Fellowship, Eli Lilly Graduate Fellowship in Chemistry); PA Cole (NIH NIGMS, R37-GM62437); SLS (NIGMS, R35-GM127045); BKW (Ono Pharma Foundation; NIH NIDDK, U01-DK123717); SS (NIH NIGMS, R35-GM122547). The authors gratefully acknowledge the use of the Opera Phenix High-Content/High-Throughput imaging system at the Broad Institute, funded by the NIH S10 grant

OD026839. This research was supported in part by the Intramural/Extramural research program of the NCATS, NIH.

The Structural Genomics Consortium is a registered charity (#1097737) that receives funds from AbbVie, Bayer Pharma AG, Boehringer Ingelheim, Canada Foundation for Innovation, Eshelman Institute for Innovation, Genome Canada through Ontario Genomics Institute [OGI-055], Innovative Medicines Initiative (EU/EFPIA) [ULTRA-DD grant no. 115766], Janssen, Merck & Co., Novartis Pharma AG, Ontario Ministry of Research, Innovation and Science (MRIS), Pfizer, São Paulo Research Foundation-FAPESP, Takeda, and the Wellcome Trust. The funders had no role in study design, data collection and analysis, decision to publish, or preparation of the manuscript. The opinions or assertions contained herein belong to the authors and are not necessarily the official views of the funders.

Conflicting interests

PA Cole is a cofounder of Acylin Therapeutics and has been a consultant to AbbVie which have had research programs in KAT inhibitors. AEC has ownership interest in, and serves on the Scientific Advisory Board of, Recursion which uses image-based data for drug discovery. PA Clemons is an advisor for Pfizer, Inc., and Belharra Therapeutics. The other authors hereby declare no conflicting interests pertaining to the material in this manuscript.

Author contributions

Designed experiments: JLD, BKH. Performed KAT inhibitor interference profiling: JLD, JHS, MC, FL, MC. Performed CP: JLD, SDN. Analyzed CP data: BKH, JLD, MJW, AA, SS, AEC, PA Clemons, BKW. Uploaded data to IDR: LPWC, AA. Performed DLS: PL. Performed cellular histone profiling: BEZ, ELF, DBL, MS. Performed U-2 OS live-cell imaging and cellular health assays: JLD. Provided key reagents, supplies, or instrumentation: PJB, TT, PA Cole, MAW,

SLS, BKW. Authored the paper: JLD. Analyzed the data: JLD, BKH, BKW. Contributed with revisions: all authors.

References

1. Arrowsmith, C.H. *et al.* The promise and peril of chemical probes. *Nat. Chem. Biol.* **11**, 536–541 (2015).
2. Dahlin, J.L. *et al.* PAINS in the assay: chemical mechanisms of assay interference and promiscuous enzymatic inhibition observed during a sulfhydryl-scavenging HTS. *J. Med. Chem.* **58**, 2091–2113 (2015).
3. Vincent, F. *et al.* Hit triage and validation in phenotypic screening: considerations and strategies. *Cell Chem. Biol.* (2020).
4. Eaton, J., Ruberto, R., Kramm, A., Viswanathan, V. & Schreiber, S. Diacylfuroxans are masked nitrile oxides that inhibit GPX4 covalently. *J. Am. Chem. Soc.* **141**, 20407–20415 (2019).
5. Eaton, J.K. *et al.* Selective covalent targeting of GPX4 using masked nitrile-oxide electrophiles. *Nat. Chem. Biol.* **16**, 497–506 (2020).
6. Gustafsdottir, S. *et al.* Multiplex cytological profiling assay to measure diverse cellular states. *PLOS ONE* **8**, e80999 (2013).
7. Bray, M. *et al.* Cell Painting, a high-content image-based assay for morphological profiling using multiplexed fluorescent dyes. *Nat. Protoc.* **11**, 1757–1774 (2016).
8. Chandrasekaran, S.N., Ceulemans, H., Boyd, J.D. & Carpenter, A.E. Image-based profiling for drug discovery: due for a machine-learning upgrade? *Nat. Rev. Drug Discov.* (2020).
9. Way, G.P. *et al.* Morphology and gene expression profiling provide complementary information for mapping cell state. *bioRxiv*, 2021.10.21.465335 (2021).
10. Schneidewind, T. *et al.* Morphological profiling identifies a common mode of action for small molecules with different targets. *Chembiochem* **21**, 3197–3207 (2020).
11. Foley, D.J. *et al.* Phenotyping reveals targets of a pseudo-natural-product autophagy inhibitor. *Angew. Chem. Int. Ed. Engl.* **59**, 12470–12476 (2020).
12. Laraia, L. *et al.* Image-based morphological profiling identifies a lysosomotropic, iron-sequestering autophagy inhibitor. *Angew. Chem. Int. Ed. Engl.* **59**, 5721–5729 (2020).
13. Hughes, R.E. *et al.* High-content phenotypic profiling in esophageal adenocarcinoma identifies selectively active pharmacological classes of drugs for repurposing and chemical starting points for novel drug discovery. *SLAS Discov.*, 2472555220917115 (2020).
14. Gerry, C. *et al.* Real-time biological annotation of synthetic compounds. *J. Am. Chem. Soc.* **138**, 8920–8927 (2016).
15. Melillo, B. *et al.* Synergistic effects of stereochemistry and appendages on the performance diversity of a collection of synthetic compounds. *J. Am. Chem. Soc.* **140**, 11784–11790 (2018).
16. Christoferow, A. *et al.* Design, synthesis, and phenotypic profiling of pyrano-furo-pyridone pseudo natural products. *Angew. Chem. Int. Ed. Engl.* **58**, 14715–14723 (2019).
17. Hippman, R.S. *et al.* Multiple chemical features impact biological performance diversity of a highly active natural product-inspired library. *Chembiochem* **21**, 3137–3145 (2020).
18. Nyffeler, J. *et al.* Bioactivity screening of environmental chemicals using imaging-based high-throughput phenotypic profiling. *Toxicol. Appl. Pharmacol.* **389**, 114876 (2020).
19. Dahlin, J.L. *et al.* Nuisance compounds in cellular assays. *Cell Chemical Biology* **28**, 356–370 (2021).
20. Nyffeler, J. *et al.* Bioactivity screening of environmental chemicals using imaging-based high-throughput phenotypic profiling. *Toxicol. Appl. Pharm.* **389**, 114876 (2020).

21. Trapotsi, M.-A. *et al.* Cell morphological profiling enables high-throughput screening for PROteolysis TArgeting Chimera (PROTAC) phenotypic signature. *bioRxiv*, 2022.01.17.476610 (2022).
22. Su, R., Xiong, S., Zink, D. & Loo, L.H. High-throughput imaging-based nephrotoxicity prediction for xenobiotics with diverse chemical structures. *Arch Toxicol* **90**, 2793–2808 (2016).
23. Lee, J.-Y.J., Miller, J.A., Basu, S., Kee, T.-Z.V. & Loo, L.-H. Building predictive in vitro pulmonary toxicity assays using high-throughput imaging and artificial intelligence. *Archives of Toxicology* **92**, 2055–2075 (2018).
24. Way, G.P. *et al.* Predicting cell health phenotypes using image-based morphology profiling. *Molecular Biology of the Cell* **32**, 995–1005 (2021).
25. Bray, M. *et al.* A dataset of images and morphological profiles of 30,000 small-molecule treatments using the Cell Painting assay. *GigaScience* **6**, 1–5 (2017).
26. Inglese, J. *et al.* Quantitative high-throughput screening: a titration-based approach that efficiently identifies biological activities in large chemical libraries. *Proc. Nat. Acad. Sci. U.S.A.* **103**, 11473–11478 (2006).
27. Zhang, T., Hatcher, J., Teng, M., Gray, N. & Kostic, M. Recent advances in selective and irreversible covalent ligand development and validation. *Cell Chem. Biol.* **26**, 1486–1500 (2019).
28. Jorda, R. *et al.* How selective are pharmacological inhibitors of cell-cycle-regulating cyclin-dependent kinases? *J. Med. Chem.* **61**, 9105–9120 (2018).
29. Tran, K. *et al.* A comparative assessment study of known small-molecule Keap1-Nrf2 protein-protein interaction inhibitors: chemical synthesis, binding properties, and cellular activity. *J. Med. Chem.* **62**, 8028–8052 (2019).
30. Henry, R. *et al.* Discordant effects of putative lysine acetyltransferase inhibitors in biochemical and living systems. *Cells* **8**, E1022 (2019).
31. Dahlin, J.L. *et al.* Assay interference and off-target liabilities of reported histone acetyltransferase inhibitors. *Nat. Commun.* **8**, 1527 (2017).
32. Dekker, F. & Haisma, H. Histone acetyl transferases as emerging drug targets. *Drug Discov. Today* **14**, 942–948 (2009).
33. Burgess, R.J. & Zhang, Z. Histone chaperones in nucleosome assembly and human disease. *Nat. Struct. Mol. Biol.* **20**, 14–22 (2013).
34. Baell, J. & Miao, W. Histone acetyltransferase inhibitors: where art thou? *Future Med. Chem.* **8**, 1525–1528 (2016).
35. Lasko, L. *et al.* Discovery of a selective catalytic p300/CBP inhibitor that targets lineage-specific tumours. *Nature* **550**, 128–132 (2017).
36. Michaelides, M. *et al.* Discovery of spiro oxazolidinediones as selective, orally bioavailable inhibitors of p300/CBP histone acetyltransferases. *ACS Med. Chem. Lett.* **9**, 28–33 (2017).
37. Baell, J. *et al.* Inhibitors of histone acetyltransferases KAT6A/B induce senescence and arrest tumour growth. *Nature* **560**, 253–257 (2018).
38. Wilson, J.E. *et al.* Discovery of CPI-1612: a potent, selective, and orally bioavailable EP300/CBP histone acetyltransferase inhibitor. *ACS Med. Chem. Lett.* (2020).
39. MacPherson, L. *et al.* HBO1 is required for the maintenance of leukaemia stem cells. *Nature* **577**, 266–270 (2020).
40. Vincent, F. *et al.* Developing predictive assays: the phenotypic screening “rule of 3”. *Sci. Transl. Med.* **7**, 293ps15 (2015).
41. Canham, S.M. *et al.* Systematic chemogenetic library assembly. *Cell Chem. Biol.* (2020).
42. Hansson, P. *et al.* A comparative study of fluorescence assays in screening for BRD4. *Assay Drug Dev. Technol.* **16**, 372–383 (2018).
43. Kroll, M.H. & Elin, R.J. Interference with clinical laboratory analyses. *Clin. Chem.* **40**, 1996–2005 (1994).
44. Dahlin, J. & Walters, M. The essential roles of chemistry in high-throughput screening triage. *Future Med. Chem.* **6**, 1265–1290 (2014).

45. Wawer, M. *et al.* Toward performance-diverse small-molecule libraries for cell-based phenotypic screening using multiplexed high-dimensional profiling. *Proc. Nat. Acad. Sci. U.S.A.* **111**, 10911–10916 (2014).
46. Swinney, D.C. & Anthony, J. How were new medicines discovered? *Nat. Rev. Drug Discov.* **10**, 507–519 (2011).
47. Solinski, H.J. *et al.* Inhibition of natriuretic peptide receptor 1 reduces itch in mice. *Sci. Transl. Med.* **11**, eaav5464 (2019).
48. Judson, R. *et al.* Editor's highlight: analysis of the effects of cell stress and cytotoxicity on *in vitro* assay activity across a diverse chemical and assay space. *Toxicol. Sci.* **152**, 323–339 (2016).
49. Escher, B.I., Henneberger, L., König, M., Schlichting, R. & Fischer, F.C. Cytotoxicity burst? Differentiating specific from nonspecific effects in Tox21 *in vitro* reporter gene assays. *Environ. Health Perspect.* **128**, 77007 (2020).
50. Niederlein, A., Meyenhofer, F., White, D. & Bickle, M. Image analysis in high-content screening. *Comb. Chem. High Throughput Screen.* **12**, 899–907 (2009).
51. Williams, E. *et al.* The Image Data Resource: A bioimage data integration and publication platform. *Nat. Methods* **14**, 775–781 (2017).
52. Hofmarcher, M., Rumetshofer, E., Clevert, D.A., Hochreiter, S. & Klambauer, G. Accurate prediction of biological assays with high-throughput microscopy images and convolutional networks. *J. Chem. Inf. Model.* **59**, 1163–1171 (2019).
53. Simm, J. *et al.* Repurposing high-throughput image assays enables biological activity prediction for drug discovery. *Cell Chem. Biol.* **25**, 611–618.e3 (2018).
54. Nyffeler, J. *et al.* Comparison of approaches for determining bioactivity hits from high-dimensional profiling data. *SLAS Discov.*, 2472555220950245 (2020).
55. Adams, C.L. *et al.* Compound classification using image-based cellular phenotypes. *Methods Enzymol.* **414**, 440–468 (2006).
56. Futamura, Y. *et al.* Morphobase, an encyclopedic cell morphology database, and its use for drug target identification. *Chem. Biol.* **19**, 1620–1630 (2012).
57. Tanaka, M. *et al.* An unbiased cell morphology-based screen for new, biologically active small molecules. *PLoS Biol.* **3**, e128 (2005).
58. Reisen, F. *et al.* Linking phenotypes and modes of action through high-content screen fingerprints. *ASSAY Drug Dev. Technol.* **13**, 415–427 (2015).
59. Willis, C., Nyffeler, J. & Harrill, J. Phenotypic profiling of reference chemicals across biologically diverse cell types using the cell painting assay. *SLAS Discov.* **25**, 755–769 (2020).
60. Hughes, R.E. *et al.* High-content phenotypic profiling in esophageal adenocarcinoma identifies selectively active pharmacological classes of drugs for repurposing and chemical starting points for novel drug discovery. *SLAS Discov.* **25**, 770–782 (2020).
61. Warchal, S.J., Dawson, J.C. & Carragher, N.O. Evaluation of machine learning classifiers to predict compound mechanism of action when transferred across distinct cell lines. *SLAS Discov.* **24**, 224–233 (2019).
62. Wolpaw, A.J. *et al.* Modulatory profiling identifies mechanisms of small molecule-induced cell death. *Proc. Nat. Acad. Sci. U.S.A.* **108**, E771–E780 (2011).
63. Ibáñez, G. *et al.* Evaluation of compound optical interference in high-content screening. *SLAS Discov.* **23**, 321–329 (2017).
64. Johnston, P.A. *et al.* Development and implementation of a high-throughput high-content screening assay to identify inhibitors of androgen receptor nuclear localization in castration-resistant prostate cancer Cells. *Assay Drug Dev. Technol.* **14**, 226–239 (2016).
65. Skuta, C. *et al.* Probes & Drugs Portal: an interactive, open data resource for chemical biology. *Nat. Methods* **14**, 759–760 (2017).
66. Corsello, S. *et al.* The Drug Repurposing Hub: a next-generation drug library and information resource. *Nat. Med.* **23**, 405–408 (2017).

67. Kametsky, L. *et al.* Improved structure, function and compatibility for CellProfiler: modular high-throughput image analysis software. *Bioinformatics* **27**, 1179–1180 (2011).
68. Hutz, J. *et al.* The multidimensional perturbation value. *J. Biomol. Screen.* **18**, 367–377 (2013).
69. Mamontova, A., Bogdanov, A. & Lukyanov, K. Influence of cell growth conditions and medium composition on EGFP photostability in live cells. *BioTechniques* **58**, 258–261 (2015).
70. Gagnon, R.C. & Peterson, J.J. Estimation of confidence intervals for area under the curve from destructively obtained pharmacokinetic data. *J Pharmacokinet Biopharm* **26**, 87-102 (1998).
71. Sorum, A.W. *et al.* Microfluidic mobility shift profiling of lysine acetyltransferases enables screening and mechanistic analysis of cellular acetylation inhibitors. *ACS Chem. Biol.* **11**, 734–741 (2015).
72. Dahlin, J. *et al.* ALARM NMR for HTS triage and chemical probe validation. *Curr. Protoc. Chem. Biol.* **10**, 91–117 (2018).
73. Dahlin, J.L. *et al.* A cell-free fluorometric high-throughput screen for inhibitors of Rtt109-catalyzed histone acetylation. *PLOS ONE* **8**, e78877 (2013).
74. Feng, B.Y. & Shoichet, B.K. A detergent-based assay for the detection of promiscuous inhibitors. *Nat. Protoc.* **1**, 550–553 (2006).
75. Usher, K., Blaszcak, L., Weston, G., Shoichet, B. & Remington, S. Three-dimensional structure of AmpC beta-lactamase from *Escherichia coli* bound to a transition-state analogue: possible implications for the oxyanion hypothesis and for inhibitor design. *Biochemistry* **37**, 16082–16092 (1998).
76. Duan, D., Doak, A., Nedyalkova, L. & Shoichet, B. Colloidal aggregation and the *in vitro* activity of traditional Chinese medicines. *ACS Chem. Biol.* **10**, 978–988 (2015).
77. Johnston, P.A. *et al.* Development of a 384-well colorimetric assay to quantify hydrogen peroxide generated by the redox cycling of compounds in the presence of reducing agents. *ASSAY Drug Dev. Technol.* **6**, 505–518 (2008).
78. Mirkovic, B., Sosic, I., Gobec, S. & Kos, J. Redox-based inactivation of cysteine cathepsins by compounds containing the 4-aminophenol moiety. *PLOS ONE* **6**, e27197 (2011).
79. Soares, K.M. *et al.* Profiling the NIH Small Molecule Repository for compounds that generate H₂O₂ by redox cycling in reducing environments. *Assay Drug Dev. Technol.* **8**, 152–174 (2010).
80. Simeonov, A. *et al.* Fluorescence spectroscopic profiling of compound libraries. *J. Med. Chem.* **51**, 2363–2371 (2008).

Figure 1. Characterization of cell injury compounds using cell painting. 205 compounds associated with cell injury were each profiled by CP after 24 h of compound exposure in U-2 OS cells. (a) Active (Mahalanobis distance) CP compounds are enriched for decreased cell number in a historical dataset²⁵. (b) Left: PCA plots showing unsupervised hierarchical clustering of CP phenotypes into nine clusters; some annotated when grossly associated with a compound category. Right: reduced feature summaries for each cluster (all compound concentrations). (c) “Dot plot” summary of cell injury compound categories by each CP cluster. (d) Clusters of cell injury compounds correlate with cell number. (e) Compounds from historical dataset with high correlation (MLI-HC) to gross injury signature (cluster 9) are active upon re-testing. Inset: heatmap and dendrogram shows pairwise correlation coefficients between each MLI CP compound profile and each of the 9 clusters (red arrowhead, enrichment of cluster 9) (f) Select CP profiles of cellular injury compounds; rainbow plots denote assigned cluster at each compound concentration; arrow indicates compound concentration of representative image. Image scales: 50 μ m.

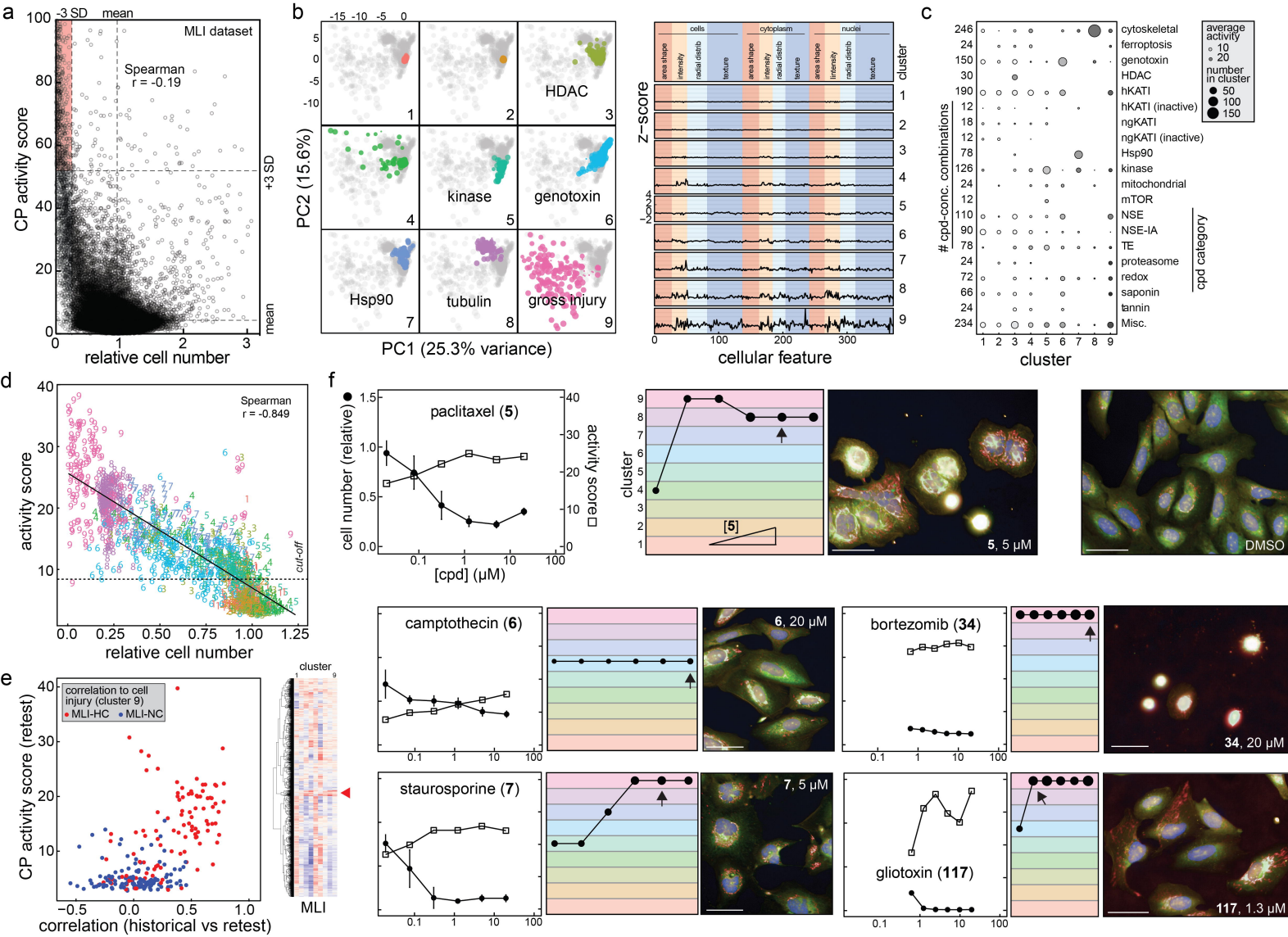
Figure 2. Nonspecific electrophiles and select targeted electrophiles produce cellular injury phenotypes in cell painting. (a) Nonspecific electrophiles (NSEs) and select targeted electrophiles (TEs) perturb cell number, are scored as bioactive in CP, and occupy gross injury feature-spaces. (b) Reduced CP feature summaries for NSEs and TEs. (c) Select CP profiles of NSEs and TEs. Note the tested electrophiles demonstrate gross cell injury at micromolar, but not nanomolar, compound concentrations. Image scales: 50 μ m.

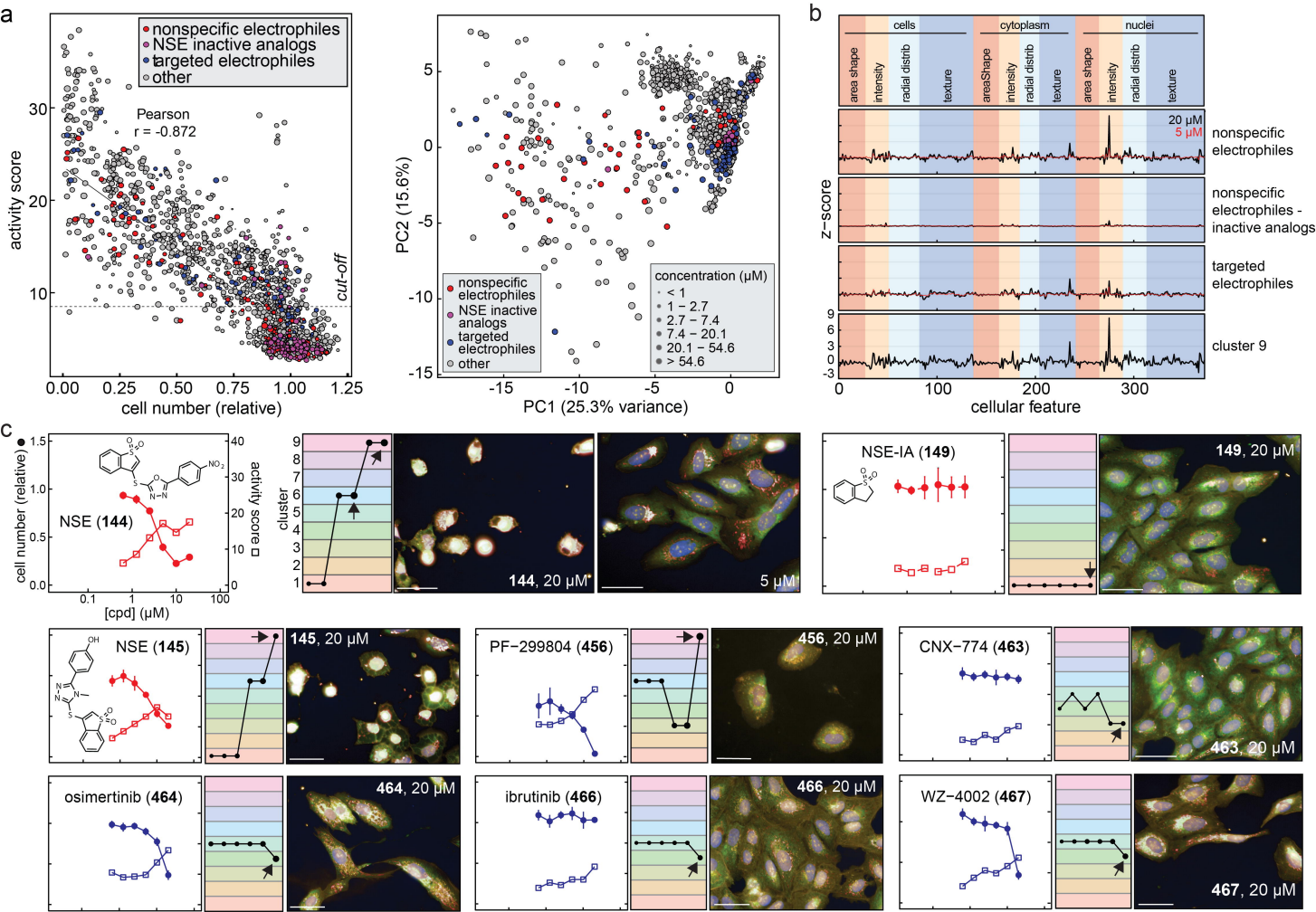
Figure 3. Historical but not next-generation KAT inhibitors produce gross injury phenotypes in cell painting. Compared to ngKATIs, many hKATIs are associated with assay interferences, suboptimal specificity, and cytotoxicity. (a) Most hKATIs but not ngKATIs perturb cell number and are scored as bioactive in CP and occupy different feature-spaces by PCA. (b) Reduced CP feature summaries for hKATIs and ngKATIs. (c) Select CP profiles of KAT inhibitors. Image scales: 50 μ m.

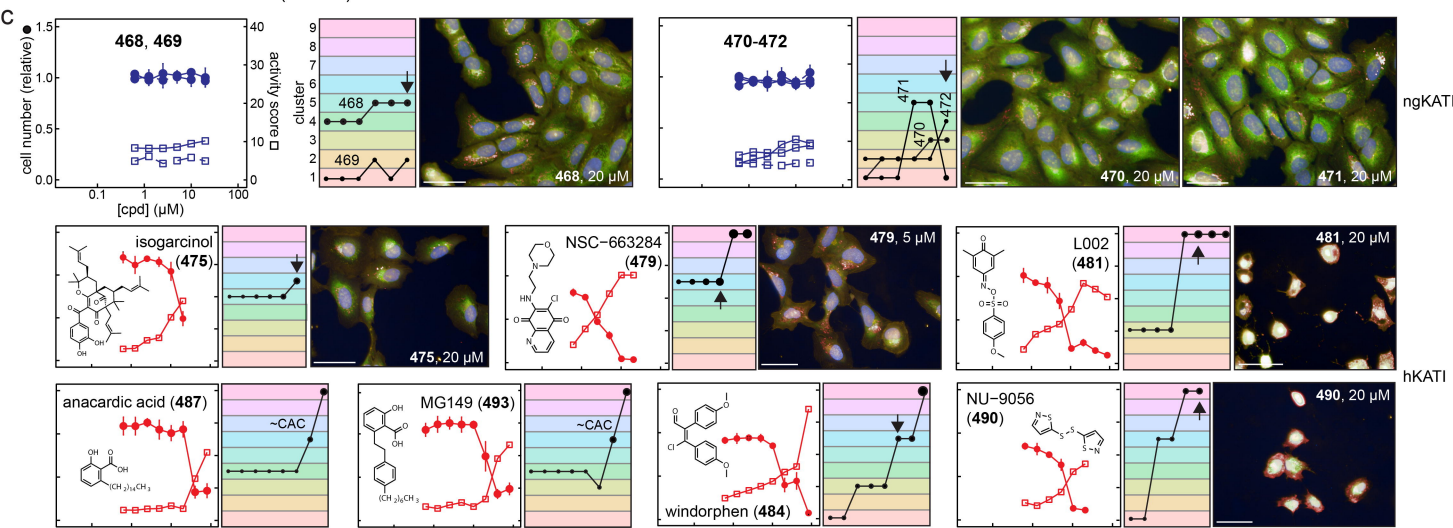
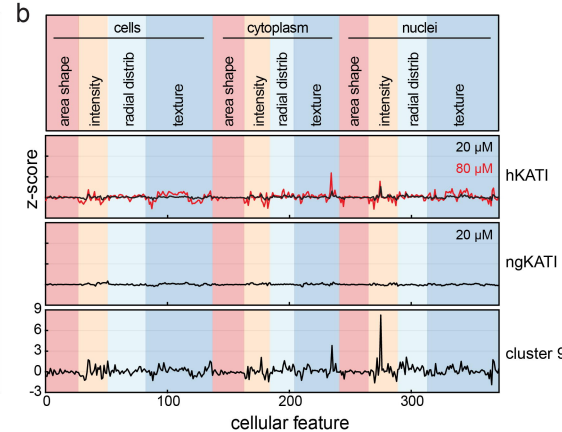
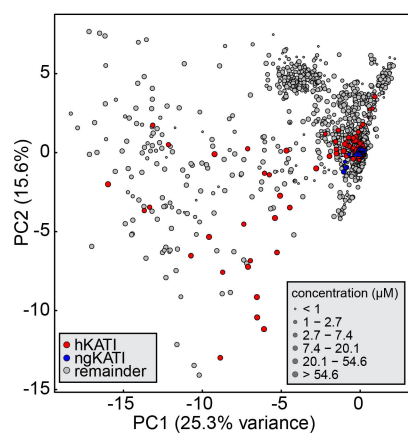
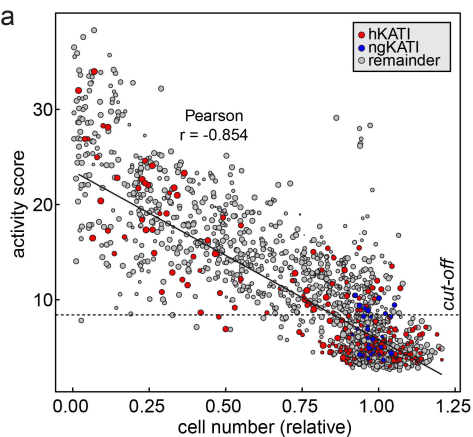
Figure 4. Cellular health and cell painting phenotypes are correlated. Compounds tested in CP were profiled for cellular health biomarkers under CP-like conditions. (a) CP activities and relative cell numbers correlate with cellular confluence, caspase 3/7 activation, and cell viability after 24 h compound treatment as measured by live-cell imaging. AUCs were calculated from the live-cell imaging assay concentration-response curves for each compound. (b) Breakdown of live-cell imaging cellular health profiles (AUC) by CP phenotypic clusters and cell injury compound groups. Object count indicates the number of cells (“objects”) above the signal threshold for each biomarker. (c) Select live-cell imaging profiles for cellular health. (d) Cell injury compounds, most notably electrophiles, decrease the intracellular GSH:GSSG ratio.

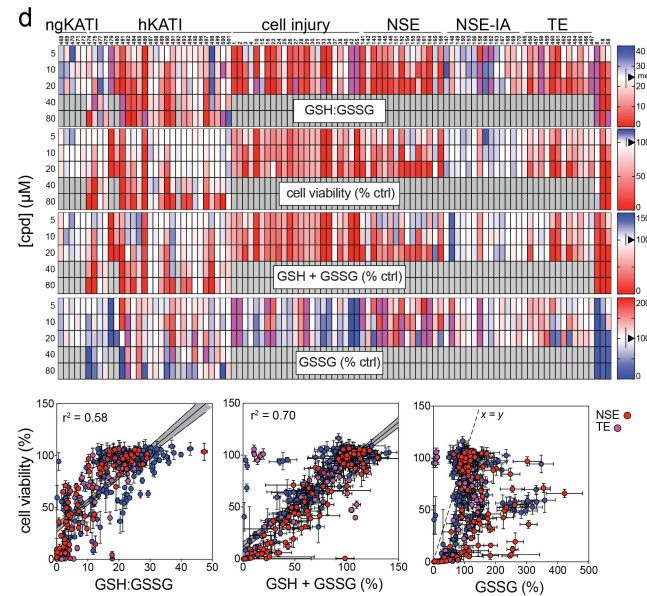
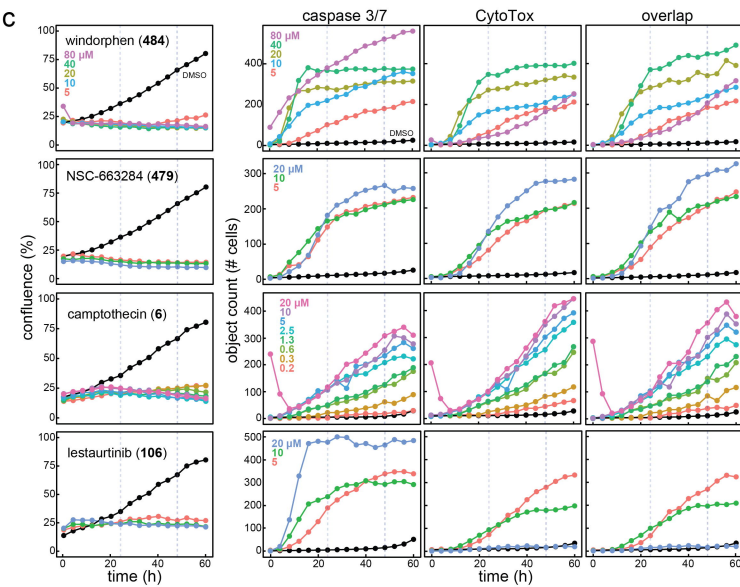
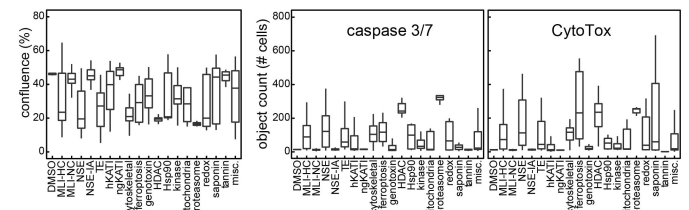
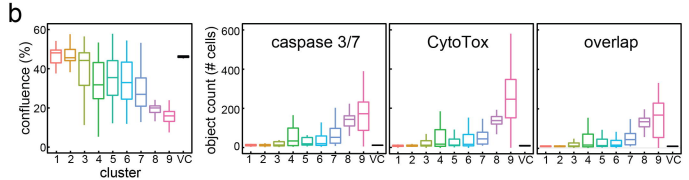
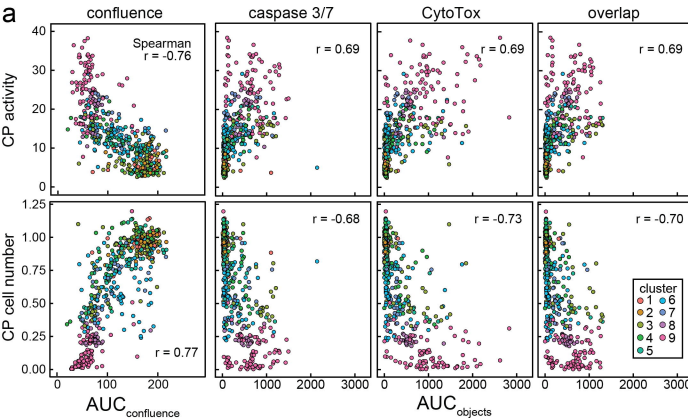
Figure 5. Additional analysis of cell injury compounds in cell painting. (a) CP phenotypes after 24- and 48-h compound treatments are correlated. (b) Replicates of active CP compounds are correlated at 24- and 48-h compound treatment times. The replicate correlation is defined by the average correlation between each replicate pair (6 comparisons total). There are generally a strong correlations between compound treatments with strong signals. (c) CP clusters from 24- and 48-h compound treatments are correlated. The horizontal- and vertical-axis correspond to the correlation of the 9 clusters to the 24- and 48-h treatment profiles, respectively. (d) CP profiles from 24- and 48-h compound treatments are correlated. Tanglegram shows connections between compound treatments from 24- and 48-treatment dendrograms. (e) Cellular health biomarkers (AUC) are grossly correlated at 24- and 48-h treatment times. N.B., while many points lie along the parity line, some have larger values at 48 h. (f) Select CP profiles comparing 24- and 48-h compound treatments.

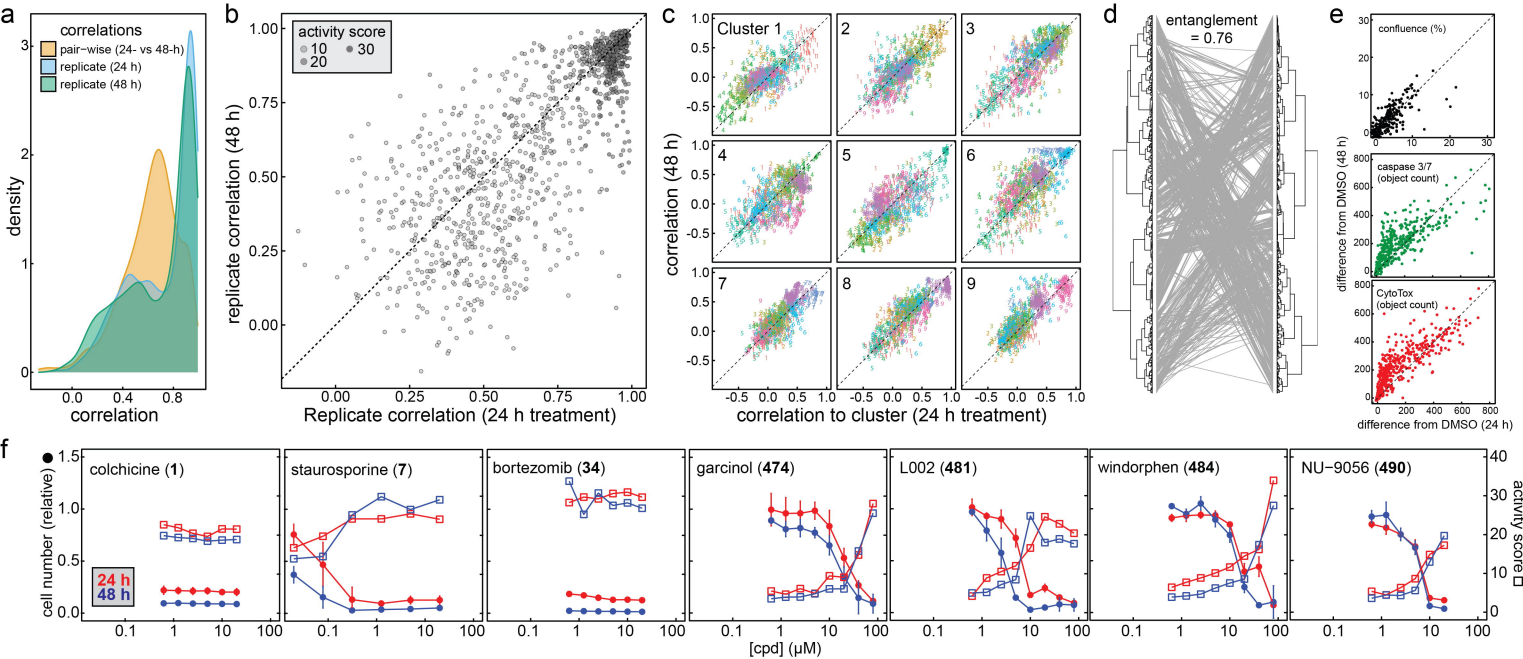
Figure 6. Proposed nuisance compound informer set for use in HCS assays. Left: an informer set can be assembled using representative compounds from key cellular injury and nuisance MoAs. Right: When an informer set is used during the assay optimization phase, more optimal experimental conditions can be selected to reduce the incidence of unwanted MoAs such as nonspecific electrophiles. When an informer set is used compound prioritization phase (“hit picking”, “HTS triage”), compounds sharing phenotypes with unwanted MoAs can be prioritized according to the desired compound characteristics.

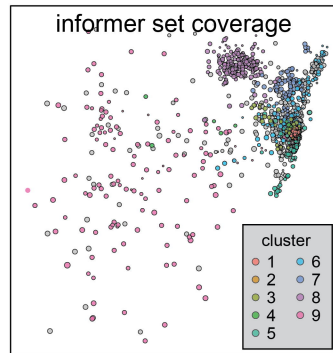
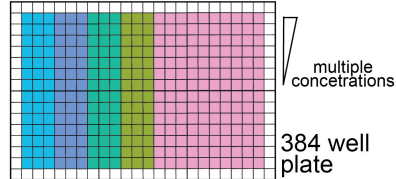
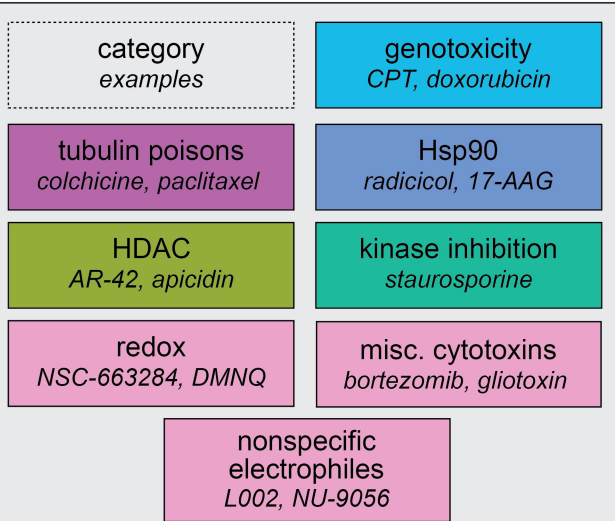












example uses
→

